




# Miniature line-scanned dual-axis confocal microscope for versatile clinical use

KEVIN W. BISHOP,<sup>1,2,†</sup>  BINGWEN HU,<sup>2,†</sup> RAJAT VYAWHARE,<sup>2,†</sup>  
ZELIN YANG,<sup>2,†</sup> DAVID C. LIANG,<sup>2</sup> GAN GAO,<sup>2</sup> ELENA  
BARAZNENOK,<sup>1,2</sup> QINGHUA HAN,<sup>1,2</sup> LYDIA LAN,<sup>1,3</sup> SARAH S. L.  
CHOW,<sup>1</sup>  NADER SANAI,<sup>4,5</sup> AND JONATHAN T. C. LIU<sup>1,2,6,\*</sup> 

<sup>1</sup>Department of Bioengineering, University of Washington, Seattle, WA 98195, USA

<sup>2</sup>Department of Mechanical Engineering, University of Washington, Seattle, WA 98195, USA

<sup>3</sup>Department of Biology, University of Washington, Seattle, Washington 98195, USA

<sup>4</sup>Ivy Brain Tumor Center, Barrow Neurological Institute, St. Joseph's Hospital and Medical Center, Phoenix 85013, AZ, USA

<sup>5</sup>Department of Neurosurgery, Barrow Neurological Institute, St. Joseph's Hospital and Medical Center, Phoenix 85013, AZ, USA

<sup>6</sup>Department of Laboratory Medicine & Pathology, University of Washington, Seattle, WA 98195, USA

<sup>†</sup>These authors contributed equally to this work.

\*[jonliu@uw.edu](mailto:jonliu@uw.edu)

**Abstract:** A miniature optical-sectioning fluorescence microscope with high sensitivity and resolution would enable non-invasive and real-time tissue inspection, with potential use cases including early disease detection and intraoperative guidance. Previously, we developed a miniature MEMS-based dual-axis confocal (DAC) microscope that enabled video-rate optically sectioned *in vivo* microscopy of human tissues. However, the device's clinical utility was limited due to a small field of view, a non-adjustable working distance, and a lack of a sterilization strategy. In our latest design, we have made improvements to achieve a 2x increase in the field of view ( $600 \times 300 \mu\text{m}$ ) and an adjustable working distance range of  $150 \mu\text{m}$  over a wide range of excitation/emission wavelengths (488–750 nm), all while maintaining a high frame rate of 15 frames per second (fps). Furthermore, the device is designed to image through a disposable sterile plastic drape for convenient clinical use. We rigorously characterize the performance of the device and show example images of *ex vivo* tissues to demonstrate the optical performance of our new design, including fixed mouse skin and human prostate, as well as fresh mouse kidney, mouse intestine, and human head and neck surgical specimens with corresponding H&E histology. These improvements will facilitate clinical testing and translation.

© 2023 Optica Publishing Group under the terms of the [Optica Open Access Publishing Agreement](#)

## 1. Introduction

Histopathology, the microscopic visualization of tissue architecture and cytological features in thinly sectioned specimens mounted on glass slides, has been the gold standard for diagnostic determinations for over a century. However, standard histology is both time-consuming (several days) and requires invasive biopsy. The invasive nature of standard biopsies is problematic for many screening applications (e.g., for epithelial cancers of the skin or oral cavity) in which the risk and cost of a biopsy procedure is often not warranted until the disease has reached an advanced and less treatable stage [1–3]. Furthermore, since only a few tissue sites are invasively biopsied from the patient, and an even smaller fraction of each biopsy is visualized by pathologists, lesions are often mischaracterized or missed entirely by histopathology. For rapid surgical guidance, frozen section analysis (FSA) is possible but faces similar limitations to standard histology in that it still takes time (30 minutes or more), requires the invasive removal of tissues, and is limited in

spatial coverage [3]. Therefore, there is potential clinical value in a portable, non-invasive method for real-time tissue histology, both for disease screening and for guiding resection procedures.

In recent decades, confocal microscopy has been investigated as a non-destructive optical-sectioning method, providing high-resolution images of fresh tissue specimens at depths of approximately 100–200  $\mu\text{m}$  (depending upon the tissue type) without requiring physical sectioning and mounting on slides [4–10]. While widefield microscopy is capable of generating high-contrast images at the very surface of fresh tissues [11–14], optical sectioning can be helpful for applications in which mucus, debris, or damage to the tissue can degrade image quality at the superficial surface, and where sub-surface imaging at depths of up to  $\sim 150 \mu\text{m}$  can help to improve image/tissue quality. Depth-resolved optical-sectioning microscopy can also provide valuable insights into the invasion of certain cancers through critical layers, such as the dermal-epidermal junction for skin cancers [15,16].

Conventional single-axis confocal (SAC) microscopes have been used ubiquitously for biological and clinical investigations. These microscopes use a common beam path for high-numerical aperture (NA) illumination and collection of light through tissues [4,6,17]. Alternatively, dual-axis confocal (DAC) microscopy employs a pair of spatially separated low-NA beams oriented towards the specimen, which has certain advantages for miniaturization [3,8,18–24] and improves optical sectioning and image contrast when imaging within highly scattering biological tissues [7,21,23,25]. In short, since the illumination and collection beams in a DAC microscope do not share an optical axis and only intersect at a localized focal region, there is improved rejection of out-of-focus and multiply scattered background light compared to standard SAC microscopes.

Conventional point-scanned SAC and DAC microscopy systems use a focused illumination beam and a collection pinhole to reject background light, creating an image by raster scanning a localized focal volume in two dimensions. Two-dimensional scanning mechanisms can complicate miniaturization due to their complexity and can limit a device's frame rate due to their reliance on point-by-point image generation. These slow frame rates often cause motion artifacts during the handheld or endoscopic use of an *in vivo* device [26]. Therefore, we have been developing line-scanned dual-axis confocal (LS-DAC) microscopes in which a focal line is rapidly scanned in only one dimension to create 2D images. By imaging the entire focal line onto a linear detector array, which also serves as a digital confocal slit, video-rate confocal imaging is achievable with a portable handheld device [10,17,22,24].

Based on several studies with our first-generation LS-DAC microscopes, we identified three major areas of improvement. First, our previous optical design achieved high spatial resolution ( $< 1\text{-}\mu\text{m}$  lateral resolution and  $< 2\text{-}\mu\text{m}$  axial resolution) at the trade-off of a limited field of view ( $\sim 300 \mu\text{m} \times 300 \mu\text{m}$ ). In practice, pathologists rarely require submicron resolution for disease-screening and surgical-guidance applications and would instead benefit from a larger field of view to better-locate and visualize patterns of malignancy in spatially heterogeneous tissues. Second, our initial prototype lacked a straightforward and dependable way of adjusting the depth of imaging within the first 100–200  $\mu\text{m}$  beneath the tissue surface. An adjustable working distance would allow clinicians to dynamically find an optimal imaging plane, which can be unpredictable due to varying levels of damage and mucosal debris at surgical margins as well as variations in the surface topology and staining characteristics of fresh tissue surfaces. Finally, our previous devices did not have a simple way to maintain sterility in a clinical setting. In this study, we introduce a second-generation handheld LS-DAC microscope, optimized based on prior preclinical and clinical feedback, to enable improved clinical usability and adoption.

## 2. Methods

### 2.1. Optical design

There are three major modules within the miniature LS-DAC microscope: the optical main body, a custom relay objective, and a detector array (Fig. 1). The laser source is selected based on

the fluorophore used in each experiment: a 488-nm fiber-coupled diode laser (Omicron LuxX 488 nm), or a 660-nm fiber-coupled diode laser (Thorlabs S1FC660). A single-mode optical fiber (Thorlabs P5-405B-PCAPC-1) introduces laser radiation into the optical main body through a custom fiber module ( $\phi = 3.2$  mm, assembled by Grintech GmbH, Germany). Within the illumination fiber module (blue beam), there are two low-NA doublets (S1 and CL) that convert the point source from the single-mode fiber to a focal line with a full width at half maximum (FWHM) length of 1.2 mm and a focusing NA of approximately 0.09. S1 is a spherical lens ( $f = 9$  mm,  $\phi = 3$  mm, Edmunds Optics catalog No. 45090). CL is a cylindrical lens ( $f = 12$  mm,  $\phi = 3$  mm) fabricated by BMV Optical Technologies based on a spherical doublet design from Edmund Optics (catalog No. 45262).

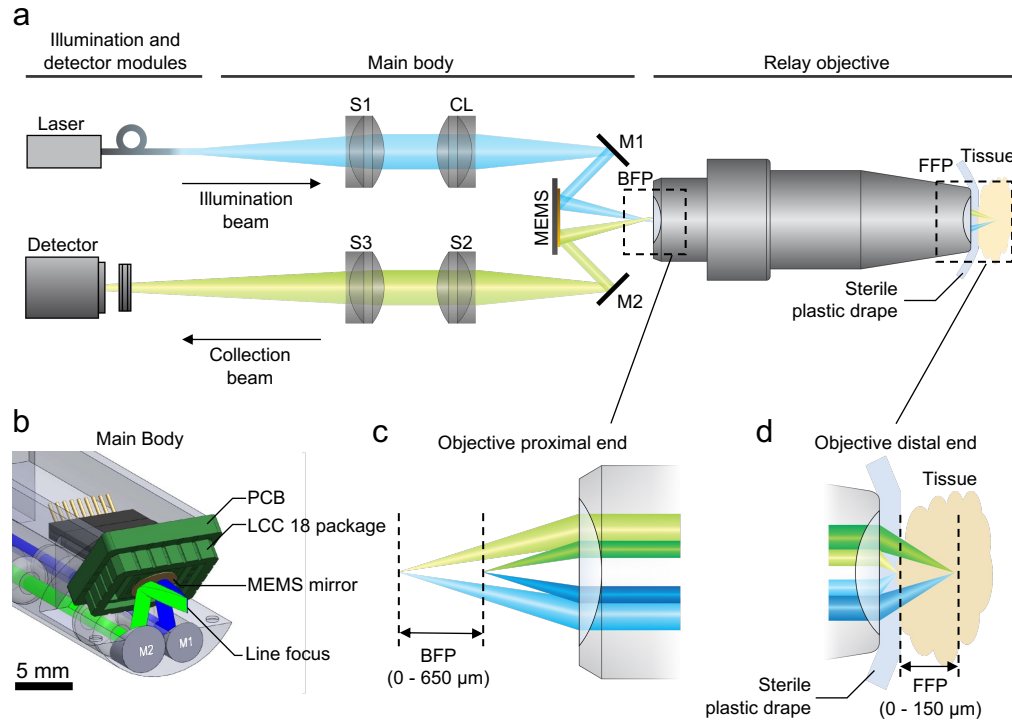


**Fig. 1.** Optical circuit of miniature LS-DAC microscope. (a) The illumination beam path (blue) and fluorescence collection beam path (green) are aligned to intersect and focus at the back focal plane (BFP) of a custom relay objective, which images the dual-axis focused beams (with 2.1x magnification) into a tissue sample placed in contact with the distal tip of the objective. A custom line-focusing fiber module, containing S1 and CL, shapes the illumination beam into a focal line at the BFP. S1, S2, and S3 are low-NA spherical doublets. CL is a low-NA cylindrical doublet. M1 and M2 are alignment mirrors. Fluorescence signal generated by the focal line within the sample is imaged back through the objective and through S2 and S3 with a combined magnification of  $\sim 10\times$  and focused onto a detector array. (b) Zoomed-in view of the LS-DAC scan head. The MEMS mirror, which is mounted in an LCC18 wire-bonded package, is soldered onto a custom PCB. The MEMS mirror scans a focal line in one direction to achieve high-framerate 2D imaging. (c) Zoomed-in view of the BFP at the proximal end of the relay objective. (d) Zoomed-in view of the front focal plane (FFP) at the objective distal end. The lens tip is designed to be covered by a plastic drape with a thickness of  $\sim 50$   $\mu\text{m}$ . The ideal axial scanning range of the BFP is 650  $\mu\text{m}$ , which causes the FFP to scan over a range of 150  $\mu\text{m}$  (starting from the outer surface of the plastic drape).

The collection beam (green beam) consists of two low-NA spherical doublets (S2:  $f = 12$  mm, Edmunds Optics catalog No. 63692; S3:  $f = 60$  mm, Edmunds Optics catalog No. 45345), both of which were reduced in diameter to 3.2 mm by BMV Optical Technologies. Collectively, these lenses image the focal line with 5x magnification from the back focal plane (BFP) of the 2.1x relay objective onto the detector array. The relay objective was custom designed by Special Optics Inc. (Rochester, NY) to maintain a small form factor, with a distal tip diameter of 9.7 mm and a total length of 49.2 mm. After the relay objective, the final effective NA in the tissue (assuming a tissue refractive index of 1.34) is 0.19 for the Gaussian illumination beam ( $1/e^2$  intensity level) and 0.30 for the uniform collection beam. With a total magnification of  $\sim 10\times$  ( $5 \times 2.1$ ), a commercial sCMOS camera (Hamamatsu ORCA Flash 4.0) with a pixel spacing of  $6.5\ \mu\text{m}$  is used to sample the focal line at near-Nyquist conditions. A digital slit is formed by cropping the sensor to a thin rectangular region of interest (ROI) measuring  $2048 \times 8$  pixels and then binning the four rows at the center of the ROI (i.e., a  $26\text{-}\mu\text{m}$  slit width, which corresponds to  $\sim 2.5\ \mu\text{m}$  within the tissue sample).

A critical feature of our newly designed relay objective is its adjustable working distance. This allows the BFP to be axially scanned, which corresponds to an axial scan of the front focal plane (FFP) within the tissue sample. The present objective has been designed to achieve diffraction-limited imaging throughout its entire focal range of  $650\ \mu\text{m}$  at the BFP, or  $150\ \mu\text{m}$  at the FFP. Furthermore, the objective lens is designed to image through a layer of plastic ( $n \sim 1.46\text{--}1.52$ ) with a thickness of  $\sim 50\ \mu\text{m}$ . For clinical use, this will allow a sterile plastic drape to be used to surround the distal tip of the relay objective lens, ensuring patient safety without relying upon a harsh and time-consuming sterilization procedure. Finally, the newly designed objective provides a large field of view of up to  $600 \times 600\ \mu\text{m}$  with low field curvature over a larger range of wavelengths (400–750 nm).

The lateral scanning mechanism for our device, which sweeps the focal line in one direction to scan a 2D *en face* (horizontal) image over time, is a commercial MEMS scanning mirror that is wire-bonded within an LCC18 package (Mirrorcle Technologies Inc.). While this MEMS scanner is capable of three degrees of freedom (tip, tilt, and pistoning), only 1D tilting is used here to scan the focal line at 15 frames per second (fps) for *en face* tissue imaging. We use two 45-deg alignment mirrors (M1, M2, fabricated by Tower Optical Inc.), which can be rotated and adjusted axially, for precise alignment of the illumination and collection foci at a half-crossing angle of 11 degrees at the BFP of the device. A 525 nm bandpass filter (Semrock 525/50-25 nm) or 721 nm bandpass filter (Semrock 721/65-25 nm) is mounted along the collection beam path to reject back-scattered illumination light. Individual  $2048 \times 8$ -pixel raw images of the focal line are transferred into the RAM of the controller PC using a frame grabber, binned into a single line ( $2048 \times 1$  pixels), and stitched into 2D images (300 lines per image) at 15 fps. Note that the raw images of the focal line can be binned with various numbers of lines (from  $2048 \times 1$  up to  $2048 \times 8$ ), which allows for a trade-off between sensitivity (signal-to-noise ratio) and axial-sectioning performance. A custom Python-based user interface was developed to display the images in real time and to enable the user to perform basic operations such as cropping, auto-gain adjustment, brightness and contrast adjustments, and video recordings.

## 2.2. Imaging procedure

The device's resolution was experimentally measured by imaging a 1951 USAF target in reflectance mode (Fig. 3). The lateral response was measured from the sharp edge of a reflective element on the USAF target, and the axial response was found by measuring the light reflected off a large reflective element on the USAF target (i.e., a flat mirror) as the target was translated axially.

The resolution uniformity (Fig. 4) was characterized by measuring  $1\text{-}\mu\text{m}$  diameter fluorescent beads embedded in a 3D agarose phantom. The beads were imaged over a shallow volume ( $\sim 100$

$\mu\text{m}$  depth range). The image of each bead was quantified with a custom algorithm that performs a 3D Gaussian fit to each bead and extracts the FWHM values in all three dimensions [27].

The drape used for resolution characterization in Fig. 3 was a sterile, medical-grade polyethylene film (3 M Steri-Drape 1000). Due to practical constraints of imaging small *ex vivo* samples, the specimens in Figs. 4–5 and Visualization 1 and Visualization 2 were imaged through a taut consumer-grade polyethylene film or standard #0 coverslip, which produced comparable results to the medical-grade drape used in Fig. 3. For measurements using a drape, a thin layer of Cargille Refractive Index Liquid ( $n_D = 1.440$ ) was applied between the objective tip and the drape to match the refractive index of the drape. In this preliminary prototype, working distance adjustment for the axial response and volumetric datasets was achieved by moving the relay objective using a linear actuator (Newport TRA12CC).

### 2.3. Tissue collection and preparation

The human prostate specimen shown in Fig. 5(a)–(b) was stained with TO-PRO-3, a nuclear dye, and optically cleared with ethyl cinnamate [28]. This tissue was de-identified prior to transfer to our lab, so this experiment did not require institutional review board approval at our institution.

The mouse skin shown in Fig. 5(d)–(f) was also stained with TO-PRO-3 and cleared with ethyl cinnamate [28]. This mouse skin was from a freshly euthanized animal donated to us by the veterinarians at our institutional animal facility, and therefore did not require institutional animal care and use committee approval.

The fresh surgical specimens shown in Fig. 5(g)–(h) and Visualization 1 were collected from patients undergoing head and neck cancer treatment at the University of Washington Medical Center. The excised tissues were stained in 1% acridine orange, which preferentially labels cell nuclei, for 1 min and rinsed in phosphate-buffered saline (PBS) to remove excess acridine orange from the tissue surface. Approval was obtained from the University of Washington Institutional Review Board [STUDY00014148] and all patients provided informed consent.

The fresh mouse tissues shown in Fig. 5(i)–(k) and Visualization 2 were again stained with 1% acridine orange for 1 min and rinsed with PBS. These mouse tissues were also from freshly euthanized animals donated by our institutional animal facility and did not require institutional animal care and use committee approval.

### 2.4. Image processing

To correct for intensity variations along the focal line and vignetting by optical components, a calibration image from a uniform fluorescein phantom was used to normalize intensity levels for the images in Fig. 5 and Visualization 1 and Visualization 2. Signal levels were subsequently normalized across raw frames for the mosaic in Fig. 5(a). Finally, a standard sharpening filter was applied. The mosaic was generated post-acquisition using MosaicJ [29], an open-source image mosaicking plug-in for ImageJ [30].

## 3. Results

A ray-trace analysis was conducted in ZEMAX to characterize the system's performance (Fig. 2). The spot diagram from the illumination path shows a root mean square (RMS) spread of  $< 2 \mu\text{m}$  across the line. This spread is within the ideal (aberration-free) line width calculated by diffraction theory ( $\text{FWHM} = 2.2 \mu\text{m}$ ), indicating near-diffraction-limited performance (Fig. 2(b)). Tilting the MEMS mirror by 5.5 degrees causes the line to shift by  $300 \mu\text{m}$  in the Y direction. Again, the spot diagram shows an RMS spread of  $< 2 \mu\text{m}$  across the line. For the collection path, the optical performance was analyzed by establishing three ideal point sources at different locations (field positions) along the focal line in tissue and performing ray-trace simulations from these sources to the detector plane (Fig. 2(c)). Near-diffraction-limited performance is achieved at the center of the field of view (e.g.,  $X = 0$  and  $150 \mu\text{m}$ ). However, the performance degrades



somewhat at the edge of the field of view (Fig. 2(d)). In the context of *in vivo* imaging, where highly scattering biological tissues make diffraction-limited imaging challenging irrespective of aberrations, this tradeoff of sacrificing some optical performance to achieve a large field of view is deemed acceptable. The relay objective was designed to minimize field curvature across this large field of view, with the objective introducing a change in focal position of  $1.5\ \mu\text{m}$  at the edge of the field of view relative to the center (Fig. 2(e)).

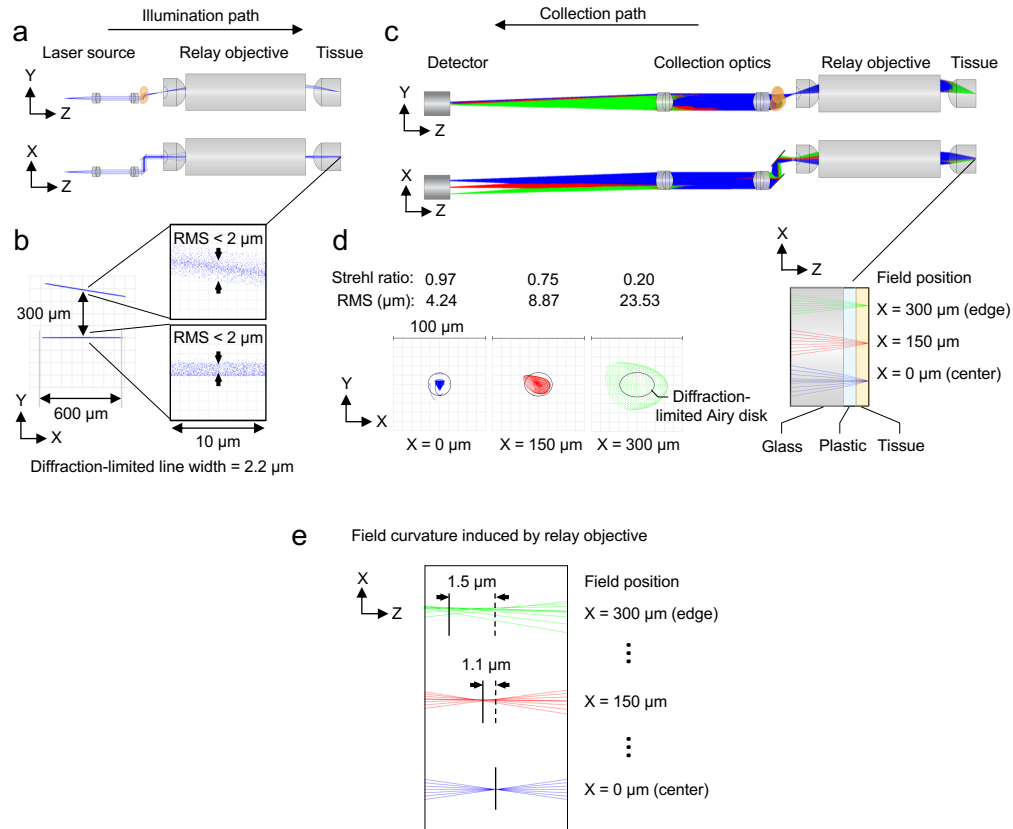


**Fig. 2.** Ray-trace simulations. (a) Illumination beam path is shown as two orthogonal views (Y-Z plane and X-Z plane). (b) Illumination spot diagrams are shown for the line focus in its centered position and at the edge of the objective's field of view when scanned by the MEMS mirror (300- $\mu\text{m}$  offset). (c) Collection beam path is shown as two orthogonal views. (d) Collection spot diagrams are shown for rays originating from three positions (field positions) along the focal line at the sample (blue:  $X = 0\ \mu\text{m}$ , red:  $X = 150\ \mu\text{m}$ , and green:  $X = 300\ \mu\text{m}$ ). The RMS spread and Strehl ratio are quantified for each case. (e) Field curvature induced by the relay objective only for the same field positions shown in (d). Note that the vertical spacing between fields in panel (e) is not to scale.

To experimentally measure the device's resolution, we imaged a USAF resolution test chart in reflectance mode. Figure 3(a) demonstrates the microscope's ability to image features at sub-cellular resolution (the line width in group 9 element 1 is  $0.98\ \mu\text{m}$ ). The field of view has also been increased to twice that of the previous device [10] with an aspect ratio of approximately 2:1, which is compatible with a 16:9 widescreen display used in many clinical procedure rooms. Additionally, we measured the lateral response and axial response of the microscope with and without a medical-grade sterile drape. The measured 20% to 80% transition width along the X-axis ( $X_{20-80}$ ) was  $0.97\ \mu\text{m}$  without the drape and  $1.17\ \mu\text{m}$  with the drape (Fig. 3(b)). The

measured FWHM at the center of the field of view was  $2.6\ \mu\text{m}$  without the drape and  $3.1\ \mu\text{m}$  with the drape (Fig. 3(c)). As shown in the log-scale axial response, the background signal levels with and without the drape are relatively similar.

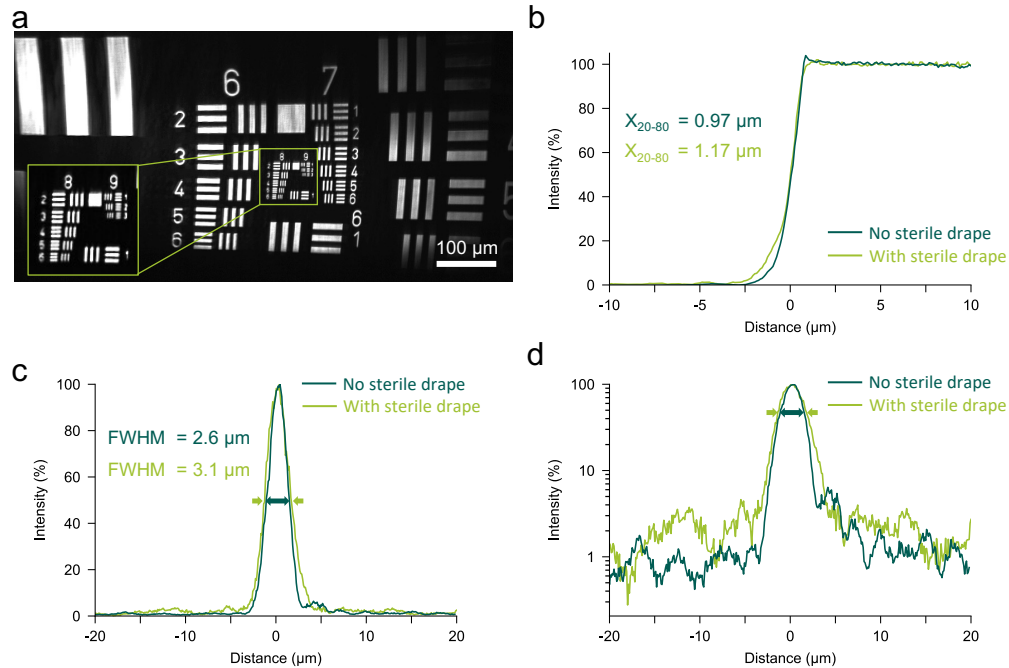


**Fig. 3.** (a) Image of reflective USAF test chart. (b) Lateral response to a chrome edge of an element on the USAF test chart with and without the sterile drape. (c) Axial response to a flat mirror plotted on a linear scale with and without the sterile drape. (d) Axial response to a flat mirror plotted on a log scale with and without the sterile drape.

As shown in Fig. 4, we also evaluated the optical performance by measuring  $1\text{-}\mu\text{m}$  diameter (i.e., nearly diffraction-limited) fluorescent beads. The FWHM of the  $1\text{-}\mu\text{m}$  beads in the lateral  $x$  dimension was  $1.7\ \mu\text{m}$  at the center of the field of view and remained relatively uniform across the entire field of view as shown in Fig. 4(b). The mean FWHM in the axial dimension (Fig. 4(c)) was  $3.35\ \mu\text{m}$  at the center of the field of view and slightly increased at the edge along the  $y$ -axis, which corresponds to the MEMS scanning direction.

The device's larger field of view and reduced field curvature ( $\sim 5\ \mu\text{m}$  total deviation in imaging depth across the field of view) relative to our previous prototype enables straightforward mosaicking of overlapping images to generate extended fields of view spanning multiple millimeters. As shown in Fig. 5(a)-(b), a mosaicked image with a lateral field of view of  $3.7 \times 1.0\ \text{mm}$  was obtained from a video sequence from *ex vivo* human prostate tissue acquired at 15 fps and shows benign prostate glands.

The device's adjustable working distance enables collection of a 3D dataset by scanning the imaging plane axially. We acquired a 3D stack of *en face* images (over a depth range from 0 to  $150\ \mu\text{m}$ ) of excised mouse skin. The resulting 3D volume shows the structural composition of the mouse skin tissue, revealing distinct layers such as the epidermis and dermis in the vertical image ( $x$ - $z$  plane) shown in Fig. 5(f). The hair follicles in the mouse skin are clearly visible in the *en face* image ( $x$ - $y$  plane) shown in Fig. 5(e).

To demonstrate our device's ability to acquire fluorescence images of fresh human tissue, we imaged fresh human head and neck (H&N) surgical resection specimens. Figures 5(g)-(h)

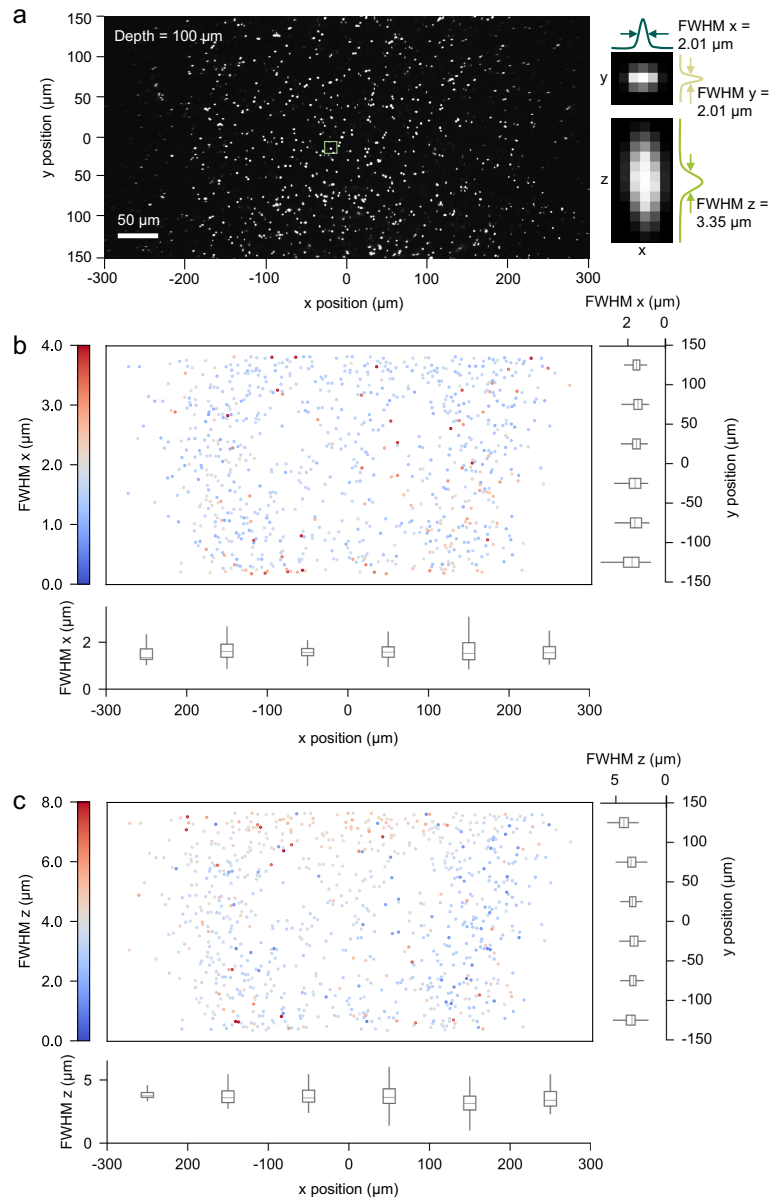


**Fig. 4.** (a) A cross-sectional image of the fluorescent microsphere phantom acquired using the DAC microscope at an image depth of 100  $\mu\text{m}$ , along with cross-sectional views of a representative bead. The FWHM dimensions of the microspheres are used to assess the spatial resolution of the system as a function of location across the field of view. (b-c) The FWHM diameter of each 1- $\mu\text{m}$  diameter fluorescent microsphere within the imaged volume is computed across the field of view. Panel (b) shows the FWHM values along the x-axis and panel (c) shows the FWHM values along the z-axis. To illustrate the uniformity of the device's spatial resolution across the field of view, box plots of the FWHM dimensions at different x and y positions are plotted alongside the color map. Each plot shows the median (centerline), 25th and 75th percentiles (box edges), and 0.1 and 99.9 percentiles (whiskers).



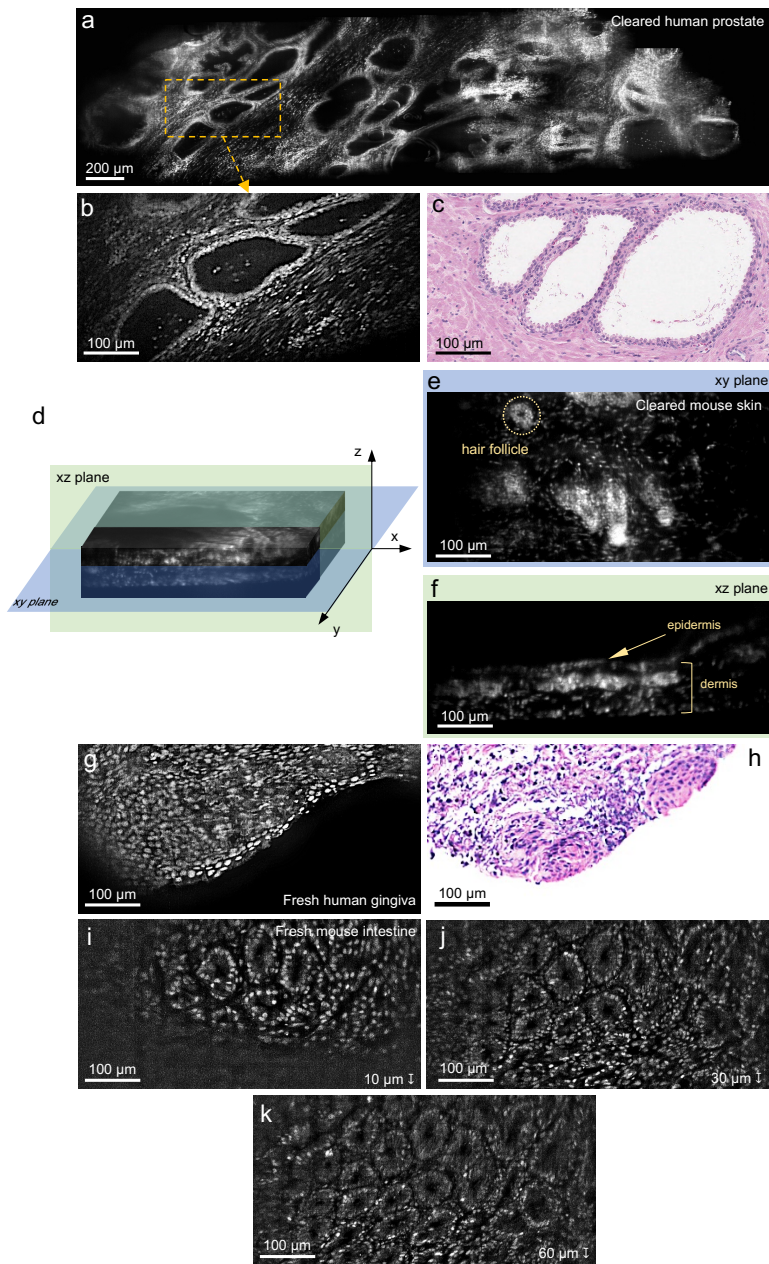


**Fig. 5.** (a) A mosaicked image of cleared prostate tissue labeled with TO-PRO-3 generated from raw frames acquired at 15 fps at a depth of  $\sim 100\ \mu\text{m}$ . (b-c) One region of interest (individual frame) is shown, accompanied by a reference archival hematoxylin and eosin (H&E) stained histology image showing similar structures. (d-f) A three-dimensional volume rendering of cleared mouse skin tissue labeled with TO-PRO-3. The XY-plane and XZ-plane images demonstrate the microscope's 3D-imaging capabilities within the mouse skin. (g-h) Freshly excised benign gingiva tissue from a human patient labeled with acridine orange, along with a corresponding H&E histology image of approximately the same tissue region. (i-k) An image stack annotated with approximate imaging depth acquired from freshly excised mouse intestine, labeled with acridine orange, showing characteristic intestinal crypts at the mucosal surface.

show benign human gingiva imaged with the miniature LS-DAC microscope with corresponding hematoxylin & eosin (H&E) histology images from approximately the same tissue region, and [Visualization 1](#) shows a continuous scan of benign human tongue.

Finally, we demonstrated the system's adjustable working distance in fresh tissue by imaging excised mouse intestine and kidney. *En face* images at sequential depths in the intestine tissue reveal the characteristic three-dimensional structure of intestinal crypts (Fig. 5(i)-(k)), and the combination of lateral scanning and depth adjustment in kidney tissue enables tracking vessel paths through the specimen ([Visualization 2](#)).

#### 4. Discussion

Previous point-scanned dual-axis confocal (PS-DAC) microscopes have exhibited a limited frame rate of up to 4 fps, achieved using complex 2D scanning mechanisms. The development of a miniature PS-DAC microscope for reliable clinical use, with reduced motion artifacts, has proven challenging due to the requirement of a MEMS-based scanner capable of high-frequency 2D scanning in the kHz range [23,31]. Although a PS-DAC architecture offers superior contrast (signal-to-background ratio) compared to a line-scanned dual-axis confocal (LS-DAC) architecture [7,8], this study demonstrates the excellent sensitivity and resolution achievable with a miniature LS-DAC microscope for high-speed imaging of fluorescently labeled fresh tissues.

Building upon our previous miniature LS-DAC microscope design, our new iteration offers an expanded field of view (double that of the previous design) while maintaining subcellular resolution that is relatively uniform across the field of view. Note that there is vignetting at the edges of the field of view due to both optical losses at the edge of the field of view and slight field curvature ( $\sim 5\text{ }\mu\text{m}$  deviation in depth across the field of view) primarily due to the scanning MEMS mirror. In other words, the curvature introduced by the objective lens, shown in Fig. 2(e), is small relative to the MEMS-induced curvature. The flat-fielding method described above significantly improves field uniformity. Additionally, the MEMS-induced curvature could in principle be corrected by implementing MEMS-mirror pistoning as previously reported [22]. Currently, the shorter dimension of the field of view is limited by the scan range of the MEMS mirror rather than the optical design, with the newly designed objective lens capable of providing a field of view up to  $600 \times 600\text{ }\mu\text{m}$ . The field of view could therefore further be expanded by optimizing the MEMS scanner. As demonstrated here, the frame rate of our device (15 fps) is adequate for real-time imaging with minimal motion artifacts and for generating large, mosaicked fields of view. However, a higher-speed detector array could be used with the existing MEMS scanning mechanism to achieve higher frame rates (if detection sensitivity is adequate).

Finally, our new design enables adjustment of the working distance of the microscope. This feature is key for future *in vivo* tissue imaging, where surface irregularities, mucous debris, or cautery and cutting damage can be present, and where a clinical user would benefit from the ability to slightly adjust the imaging plane to optimize the image quality. While our previous design allowed for some adjustment through the application of gentle pressure or by turning a threaded lens cap [10,24], these methods were cumbersome and not always effective.

In future work, we aim to fully package the primary optical components (main body and relay objective) with a compact detector array into a handheld device suitable for a range of clinical uses, such as noninvasive screening for epithelial cancers (e.g., oral cancer) or surgical guidance (e.g., glioma resections). This work introduces several optimizations that are important for clinical testing and ultimately clinical adoption.

**Funding.** National Science Foundation (DGE-1762114); National Cancer Institute (R01CA244170).

**Acknowledgments.** The authors would like to thank George Chen, Linpeng Wei, and Chengbo Yin for helpful technical discussions and Priti Lal for providing the prostate tissues shown in this manuscript.

Any opinions, findings, and conclusions or recommendations expressed in this material are those of the author(s) and do not necessarily reflect the views of the NSF, NIH, or United States government.

**Disclosures.** The authors declare that there are no conflicts of interest related to this article.

**Data availability.** The imaging datasets shown in this manuscript are not hosted publicly due to their large size and are available from the authors upon request.

## References

1. E. C. Yang, M. T. Tan, R. A. Schwarz, R. R. Richards-Kortum, A. M. Gillenwater, and N. Vigneswaran, "Noninvasive diagnostic adjuncts for the evaluation of potentially premalignant oral epithelial lesions: current limitations and future directions," *Oral Surg. Oral Med. Oral Pathol. Oral Radiol.* **125**(6), 670–681 (2018).
2. X. Duan, H. Li, F. Wang, X. Li, K. R. Oldham, and T. D. Wang, "Three-dimensional side-view endomicroscope for tracking individual cells in vivo," *Biomed. Opt. Express* **8**(12), 5533–5545 (2017).
3. K. W. Bishop, K. C. Maitland, M. Rajadhyaksha, and J. T. C. Liu, "In vivo microscopy as an adjunctive tool to guide detection, diagnosis, and treatment," *J. Biomed. Opt.* **27**(04), 040601 (2022).
4. N. D. Pilonis, W. Januszewicz, and M. di Pietro, "Confocal laser endomicroscopy in gastro-intestinal endoscopy: technical aspects and clinical applications," *Transl. Gastroenterol. Hepatol.* **7**, 7 (2022).
5. K. Vyas, M. Hughes, B. G. Rosa, and G. Yang, "Fiber bundle shifting endomicroscopy for high-resolution imaging," *Biomed. Opt. Express* **9**(10), 4649–4664 (2018).
6. A. L. Polglase, W. J. McLaren, S. A. Skinner, R. Kiesslich, M. F. Neurath, and P. M. Delaney, "A fluorescence confocal endomicroscope for in vivo microscopy of the upper- and the lower-GI tract," *Gastrointest. Endosc.* **62**(5), 686–695 (2005).
7. Y. Chen, D. Wang, and J. T. C. Liu, "Assessing the tissue-imaging performance of confocal microscope architectures via Monte-Carlo simulations," *Opt. Lett.* **37**(21), 4495–4497 (2012).
8. D. Wang, Y. Chen, Y. Wang, and J. T. C. Liu, "Comparison of line-scanned and point-scanned dual-axis confocal microscope performance," *Opt. Lett.* **38**(24), 5280–5283 (2013).
9. D. Wang, D. Meza, Y. Wang, L. Gao, and J. T. C. Liu, "Sheet-scanned dual-axis confocal microscopy using Richardson–Lucy deconvolution," *Opt. Lett.* **39**(18), 5431–5434 (2014).
10. C. Yin, A. K. Glaser, S. Y. Leigh, Y. Chen, L. Wei, P. C. S. Pillai, M. C. Rosenberg, S. Abeytunge, G. Peterson, C. Glazowski, N. Sanai, M. J. Mandella, M. Rajadhyaksha, and J. T. C. Liu, "Miniature in vivo MEMS-based line-scanned dual-axis confocal microscope for point-of-care pathology," *Biomed. Opt. Express* **7**(2), 251–263 (2016).
11. G. Matz, B. Messerschmidt, W. Göbel, S. Filser, C. S. Betz, M. Kirsch, O. Uckermann, M. Kunze, S. Flämig, A. Ehrhardt, K. Irion, M. Haack, M. M. Dorostkar, J. Herms, and H. Gross, "Chip-on-the-tip compact flexible endoscopic epifluorescence video-microscope for in-vivo imaging in medicine and biomedical research," *Biomed. Opt. Express* **8**(7), 3329–3342 (2017).
12. T. N. Ford, D. Lim, and J. Mertz, "Fast optically sectioned fluorescence HiLo endomicroscopy," *J. Biomed. Opt.* **17**(02), 1 (2012).
13. F. Fereidouni, Z. T. Harmany, M. Tian, A. Todd, J. A. Kintner, J. D. McPherson, A. D. Borowsky, J. Bishop, M. Lechpammer, S. G. Demos, and R. Levenson, "Microscopy with ultraviolet surface excitation for rapid slide-free histology," *Nat. Biomed. Eng.* **1**(12), 957–966 (2017).
14. W. Xie, Y. Chen, Y. Wang, L. Wei, C. Yin, A. K. Glaser, M. E. Fauver, E. J. Seibel, S. M. Dintzis, J. C. Vaughan, N. P. Reder, and J. T. C. Liu, "Microscopy with ultraviolet surface excitation for wide-area pathology of breast surgical margins," *J. Biomed. Opt.* **24**(02), 1 (2019).
15. J. Robic, B. Perret, A. Nkengne, M. Couprie, and H. Talbot, "Three-dimensional conditional random field for the dermal–epidermal junction segmentation," *J. Med. Imaging* **6**(02), 1 (2019).
16. A. Bozkurt, K. Kose, J. Coll-Font, C. Alessi-Fox, D. H. Brooks, J. G. Dy, and M. Rajadhyaksha, "Skin strata delineation in reflectance confocal microscopy images using recurrent convolutional networks with attention," *Sci. Rep.* **11**(1), 12576 (2021).
17. L. Wei, C. Yin, and J. T. C. Liu, "Dual-axis confocal microscopy for point-of-care pathology," *IEEE J. Sel. Top. Quantum Electron.* **25**(1), 1–10 (2019).
18. T. D. Wang, M. J. Mandella, C. H. Contag, and G. S. Kino, "Dual-axis confocal microscope for high-resolution in vivo imaging," *Opt. Lett.* **28**(6), 414–416 (2003).
19. T. D. Wang, C. H. Contag, M. J. Mandella, N. Y. Chan, and G. S. Kino, "Dual-axes confocal microscopy with post-objective scanning and low-coherence heterodyne detection," *Opt. Lett.* **28**(20), 1915–1917 (2003).
20. T. D. Wang, C. H. Contag, M. J. Mandella, N. Y. Chan, and G. S. Kino, "Confocal fluorescence microscope with dual-axis architecture and biaxial postobjective scanning," *J. Biomed. Opt.* **9**(4), 735–742 (2004).
21. J. T. C. Liu, M. J. Mandella, S. Friedland, R. Soetikno, J. M. Crawford, C. H. Contag, G. S. Kino, and T. D. Wang, "Dual-axes confocal reflectance microscope for distinguishing colonic neoplasia," *J. Biomed. Opt.* **11**(5), 054019 (2006).
22. L. Wei, C. Yin, Y. Fujita, N. Sanai, and J. T. C. Liu, "Handheld line-scanned dual-axis confocal microscope with pistoned MEMS actuation for flat-field fluorescence imaging," *Opt. Lett.* **44**(3), 671–674 (2019).
23. J. T. C. Liu, M. J. Mandella, N. O. Loewke, H. Haeblerle, H. Ra, W. Piyawattanametha, O. Solgaard, G. S. Kino, and C. H. Contag, "Micromirror-scanned dual-axis confocal microscope utilizing a gradient-index relay lens for image guidance during brain surgery," *J. Biomed. Opt.* **15**(2), 026029 (2010).

24. C. Yin, L. Wei, S. Abeytunge, G. Peterson, M. Rajadhyaksha, and J. T. C. Liu, "Label-free in vivo pathology of human epithelia with a high-speed handheld dual-axis confocal microscope," *J. Biomed. Opt.* **24**(03), 1 (2019).
25. Y. Chen and J. T. C. Liu, "Characterizing the beam steering and distortion of Gaussian and Bessel beams focused in tissues with microscopic heterogeneities," *Biomed. Opt. Express* **6**(4), 1318–1330 (2015).
26. G. Li, H. Li, X. Duan, Q. Zhou, J. Zhou, K. R. Oldham, and T. D. Wang, "Visualizing epithelial expression in vertical and horizontal planes with dual axes confocal endomicroscope using compact distal scanner," *IEEE Trans. Med. Imaging*, **36**(7), 1482–1490 (2017).
27. K. W. Bishop, L. A. E. Barner, Q. Han, E. Baraznenok, L. Lan, C. Poudel, G. Gao, R. B. Serafin, S. S. L. Chow, A. K. Glaser, A. Janowczyk, D. Brenes, H. Huang, D. Miyasato, L. D. True, S. Kang, J. C. Vaughan, and J. T. C. Liu, "An end-to-end workflow for non-destructive 3D pathology," *bioRxiv*, 2023.08.03.551845 (2023).
28. A. Klingberg, A. Hasenberg, I. Ludwig-Portugall, A. Medyukhina, L. Männ, A. Brenzel, D. R. Engel, M. T. Figge, C. Kurts, and M. Gunzer, "Fully Automated evaluation of total glomerular number and capillary tuft size in nephritic kidneys using lightsheet microscopy," *J. Am. Soc. Nephrol.* **28**(2), 452–459 (2017).
29. P. Thévenaz and M. Unser, "User-friendly semiautomated assembly of accurate image mosaics in microscopy," *Microsc Res Tech.* **70**(2), 135–146 (2007).
30. J. Schindelin, I. Arganda-Carreras, E. Frise, V. Kaynig, M. Longair, T. Pietzsch, S. Preibisch, C. Rueden, S. Saalfeld, B. Schmid, J. Tinevez, D. J. White, V. Hartenstein, K. Eliceiri, P. Tomancak, and A. Cardona, "Fiji – an Open-Source platform for biological image analysis," *Nat. Methods* **9**(7), 676–682 (2012).
31. C. L. Arrasmith, D. L. Dickensheets, and A. Mahadevan-Jansen, "MEMS-based handheld confocal microscope for in-vivo skin imaging," *Opt. Express* **18**(4), 3805–3819 (2010).